情報地質 第26巻 第2号 082-083頁 2015年
Geoinformatics, vol.26, no.2, pp.082-083, 2015

# Simulation of Hyperspectral Imagery from Landsat Imagery for Detailed Mineral Mapping

Nguyen Tien Hoang* and Katsuaki Koike*

*Graduate School of Engineering, Kyoto University, Katsura C1–2–215, Kyoto 615–8540, Japan.

E–mail: koike.katsuaki.5x@kyoto–u.ac.jp (K. Koike)

Key words: Hyperion imagery, Multivariate analysis, BMA, Spectral reconstruction

## 1. Introduction

Minerals can be detected from remotely sensed imagery by combining geologic and fracture mapping with the recognition of hydrothermally altered rocks. Generation of most epithermal vein deposits has been related to hydrothermal alteration of the adjacent country rocks (Sabins, 1999). Passive sensors were applied in geological applications, ranging from a few spectral bands to more than 100 contiguous bands, covering visible to shortwave infrared regions of the electromagnetic spectrum. Development of multi– and hyper–spectral geologic remote sensing is classified into the Landsat era, ASTER era, and hyperspectral era (van der Meer *et al.*, 2012). EO–1 Hyperion, a representative hyperspectral sensor, has been applied to map hydrothermal alteration by covering the 0.4 – 2.5 µm range with 242 bands at approximately 10 nm spectral resolution and 30 m spatial resolution. Despite this spectral superiority, its image scene is much narrower than Landsat image scene.

Based on that background, this study aims to develop a new method, Pseudo–Hyperspectral Image Synthesis Algorithm (PHISA), to transform Landsat imagery into pseudo hyperspectral imagery using the correlation between Landsat and EO–1 Hyperion data. The pseudo–hyperspectral imagery can have the number of bands as same as the number of high–quality Hyperion bands, and the same swath width as Landsat scene. The resultant pseudo–hyperspectral imagery must contribute to detailed identification of minerals than the traditional satellite imagery.

## 2. Study area and data

For a case study, we selected an area with 6 km × 7.1 km size in the southwestern Nevada volcanic field in the US, which is located about 10 km northwest of the Gold Mountain and 30 km southwest of the Cuprite alteration zones. Because of an extremely arid climate condition, this region is barren and sparsely vegetated land, which is suitable for remote sensing–based mineral mapping. Cuprite served as the test site of many remote sensing instruments including airborne and orbital visible, near–infrared, thermal–infrared, and hyperspectral sensors (Swayze *et al.*, 2014).

We used two cloud–free images on 23 July 2001, Landsat 7 ETM+ and EO–1 Hyperion images. Both satellites have the sun–synchronous orbit at an altitude of 705 km and provide Earth imagery at a 30 m spatial resolution.

## 3. Methodology

The Hyperion data should be corrected prior to any data analysis because they suffer from noise and sensor artefacts (Farifteh *et al.*, 2013). In this study, the Hyperion data were corrected for outlier pixels, vertical strips, and smile effects prior to atmospheric calibration. Both data were corrected for the atmospheric effects using ENVI–FLAASH module, and Hyperion scene was co-registered to Landsat scene.

Assuming that multivariate linear regression models can be hold between each of Hyperion bands and Landsat bands, Bayesian model averaging method (BMA) was applied to select the best model from a set of possible models. This best model is used to build pseudo–hyperspectral data which has the same swath width as the Landsat scene. A multivariate linear regression model is:

$$H_{ij} = \beta_{0i} + \beta_{1i}.L_{1j} + \beta_{2i}.L_{2j} + \beta_{3i}.L_{3j} + \beta_{4i}.L_{4j} + \beta_{5i}.L_{5j} + \beta_{6i}.L_{6j} + \varepsilon_{ij} \quad (1)$$

where $H_{ij}$ represents pixel value of Hyperion image at band $i$ and location $j$; $\beta_{0i}$ is intercept at Hyperion band $i$; $\beta_{1i}$, $\beta_{2i}$, $\beta_{3i}$, $\beta_{4i}$, $\beta_{5i}$, and $\beta_{6i}$ are unknown regression coefficients between Landsat bands and Hyperion band $i$; $L_{1j}$, $L_{2j}$, $L_{3j}$, $L_{4j}$, $L_{5j}$, and $L_{6j}$ represent pixel values at location $j$ of Landsat band 1, 2, 3, 4, 5, and 7, respectively; and $\varepsilon_{ij}$ is random error (residual) at band $i$ and location $j$.

BMA accounts for the model uncertainty inherent in the variable selection problem by averaging over the best models in the model class according to approximate posterior model probability. The posterior probability is derived by means of Bayes' theorem (Culka, 2014).

$$p(\omega|D,A,K) = \frac{p(D|\omega)p(\omega|K)}{\int_{\Omega} p(D|\omega)p(\omega|K)d\omega} \quad (2)$$

where $p(D/\omega)$ is a formal probability model for some (unknown) value of $\omega$, the probabilistic mechanism which has generated the observed data $D$; $p(\omega/K)$ is the prior probability distribution over the sample space Ω, describing the available (expert) knowledge $K$ about the value of $\omega$ prior to the data being observed; and $p(\omega/D, A, K)$ is the posterior probability density. The best model shows the lowest Bayesian Information Criterion (BIC) and the highest posterior probability.

## 4. Results and discussion

Based on the model selection results by BMA, Landsat imagery was transformed into 155 bands of pseudo–hyperspectral imagery. Most models have multiple R–

squared values higher than 90%, which assures high accuracy of the models. The lowest one is 76% (Fig. 1). Band 5 of Landsat imagery appears the most frequently (152 times), while Band 7 is less frequent (105 times) in the models. Comparing the pair of images in Figure 2, there are no clear differences between the pseudo– and original data. The pattern, texture, shape, and border of objects in both images look quite similar, but the tone of color is slightly brighter in the pseudo–hyperspectral data. This difference may be caused by that we calculated the regression model for all the pixels of each band without considering classification of surface features. The transformation results would have been much better if a land cover map or a geologic map was used to find the best model of each feature at every bands.

Two boxplots of Root Mean Square Error (RMSE) and the correlation coefficients between each band of original Hyperion data and the pseudo–hyperspectral data are shown in Figure 3. Most bands have Pearson's coefficients > 0.95, and a small fraction have the coefficients < 0.93 like outliers in the data sets. Band 220 has the lowest correlation coefficient of 0.87. In a similar manner, RMSE values are mostly smaller than 0.014, which is considerably low. Because only RMSE of band 160 is 0.052, this band should be removed from further processing.

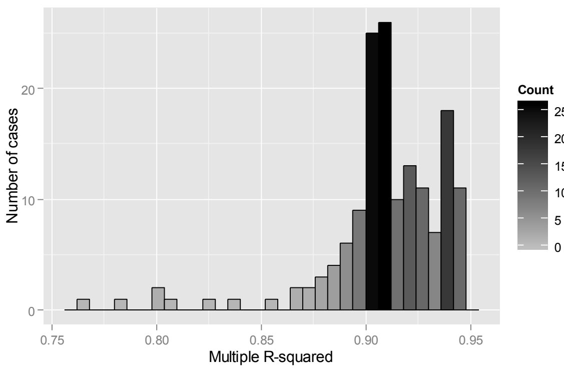

Figure 1. Histogram of multiple R–squared.

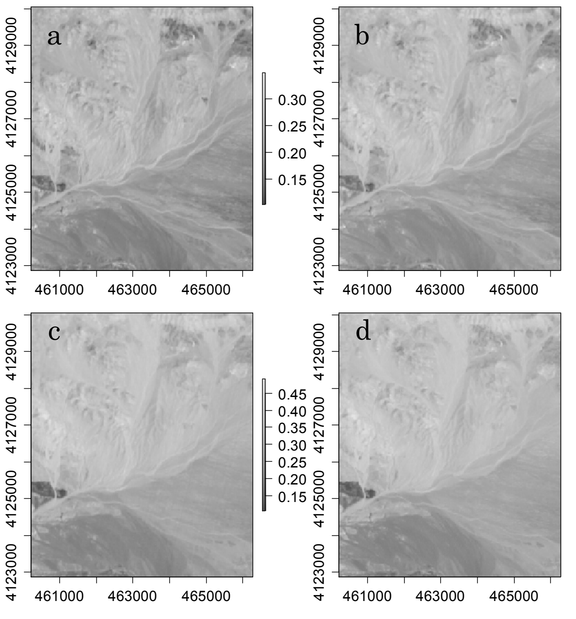

Figure 2. Visual comparison of Hyperion data (left) and pseudo– hyperspectral data (right): (a) and (b) are images of band 25, and (c) and (d) are images of band 159.

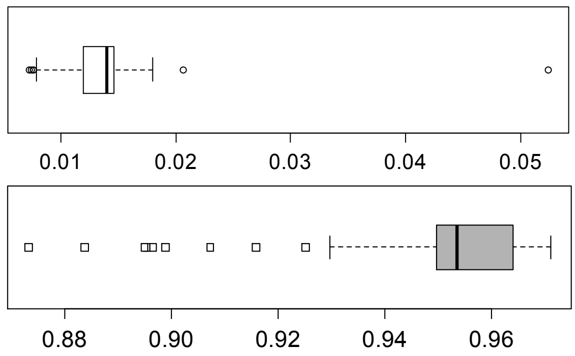

Figure 3. Boxplot of RMSE (above) and Pearson's coefficient (below) between the pseudo– and original bands.

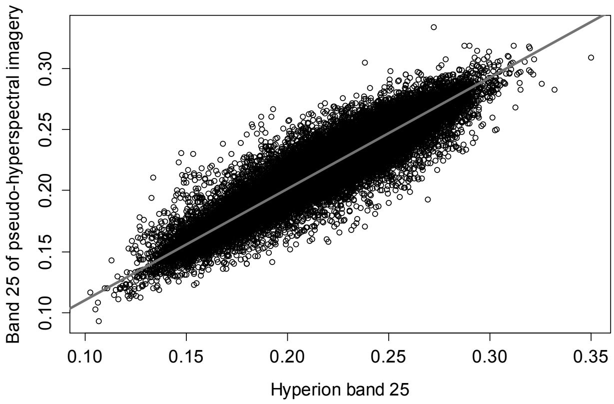

Figure 4. Scatter plot of pseudo– and original data of band 25.

Figure 4 shows a strong correlation and high linearity between pseudo– and original band 25. Most pseudo–bands have the same linearity as the band 25 with the original bands. These observations suggest that the statistical suitability of PHISA.

## 5. Conclusion

We have developed a transformation method of Landsat imagery into pseudo–Hyperion imagery, PHISA. A total of 155 pseudo–bands are simulated with high accuracy by the multivariate linear regression models between each of Hyperion bands and Landsat bands and the Bayesian model averaging method. Strong correlations between each band of Hyperion data and the pseudo–hyperspectral data were confirmed. We are now in the process of mineral mapping using the pseudo–Hyperion imagery, and improving PHISA by searching the best model of each feature at every bands.

## References

Sabins, F. F. (1999) Remote sensing for mineral exploration. *Ore Geol. Rev.*, vol.14, pp. 157–183.

van der Meer, F. D. et al. (2012) Multi– and hyperspectral geologic remote sensing: A review. *Int. J. Appl. Earth Obs. Geoinformation.*, vol.14, pp. 112–128.

Swayze, G. A. et al. (2014) Mapping Advanced Argillic Alteration at Cuprite, Nevada, Using Imaging Spectroscopy. *Econ. Geol.*, vol.109, pp. 1179–1221.

Farifteh, J., Nieuwenhuis, W. & García–Meléndez, E. (2013) Mapping spatial variations of iron oxide by–product minerals from EO–1 Hyperion. *Int. J. Remote Sens.*, vol.34, pp. 682–699.

Culka, M. (2014) Applying Bayesian model averaging for uncertainty estimation of input data in energy modelling. *Energy Sustain. Soc.*, vol.4, pp.1–17.